Chirality-Selective Optical Scattering Force on Single-Walled Carbon Nanotubes

Susan E. Skelton Spesyvtseva,[1,*] Satoru Shoji,[1,†] and Satoshi Kawata[1,2]

[1]*Department of Applied Physics, Osaka University, 2-1 Yamadaoka, Suita, Osaka 565-0871, Japan*
[2]*RIKEN, The Institute of Physical and Chemical Research, 2-1 Hirosawa, Wako, Saitama 351-0198, Japan*

(Received 25 September 2014; revised manuscript received 14 January 2015; published 9 April 2015)

We show that optical forces acting on carbon nanotubes are substantially enhanced when the optical wavelength is tuned to resonances in the electronic band structure. Using a tunable laser source, we experimentally demonstrate a resonant optical scattering force on single-walled carbon nanotubes and, by tuning the wavelength, exploit this force to achieve chirality enrichment of four chiralities of nanotubes. Our results represent a significant step towards optical manipulation and sorting of carbon nanotubes based on their chiral vector.

DOI: 10.1103/PhysRevApplied.3.044003

I. INTRODUCTION

Single-walled carbon nanotubes (SWCNTs) attract extensive interest due to their nanoscale dimensions and exceptional material and electronic properties, promising applications as diverse as chemical and optical sensors [1,2], hydrogen storage [3–5], and energy conversion [6,7], as well as high-speed electronics [8–11] and computing [12]. However, progress towards technological applications [2,3,6,8,11,12] is impeded by the requirement for pure populations of nanotubes with identical chirality [13], which is difficult to achieve by current methods of synthesis.

SWCNTs exhibit unique optical and spectroscopic properties due to the one-dimensional quantum confinement of electronic and phonon states [14,15], resulting in van Hove singularities where the density of states tends to infinity for well-defined energy values [16]. When the energy of an incident photon matches the energy of a van Hove singularity, the resultant photophysical processes are resonantly enhanced. SWCNTs are defined by a chiral vector (n, m) which defines the wrapping angle with respect to the unit vectors in the hexagonal graphene lattice [17] and, hence, the diameters of the tube, the band structure, and the electronic and optical properties.

Here, we demonstrate a resonant optical scattering force on SWCNTs. We suggest that this force could be employed in an optical method to directly sort carbon nanotubes of arbitrary chirality based on their optoelectronic properties. By tuning the wavelength of the laser beam close to the band-gap energy, the optical force is resonantly enhanced, allowing us to experimentally demonstrate enrichment of nanotubes with a specified chiral vector.

Optical sorting, where differences in the interaction of an optical field with particles with differing physical characteristics result in a spatial separation of different types of particles [18], is a useful technique for sorting colloids based on particle size or refractive index [19]. More recently, resonant optical sorting has been studied for the optical sorting and transport of plasmonic nanoparticles [20,21]. Although preferential optical trapping of a single chirality of nanotubes in an optical tweezers has previously been demonstrated [22], here we report a resonant dependence of the optical scattering force. Furthermore, by varying the wavelength, we demonstrate the tunability of an optical force on SWCNTs and exploit this feature to realize selective arbitrary chirality enrichment of SWCNTs.

Chirality-based sorting of SWCNTs has previously been demonstrated by density gradient ultracentrifugation [23–25], ion exchange chromatography [26], gel chromatography [27], and chemical methods such as DNA wrapping [28] and conjugated polymer extraction [29], although these methods suffer from various problems including long processing times, low chiral purity, prohibitive expense, and, in the case of chemical methods, difficulty in removing wrapping molecules from sorted nanotubes. Optical sorting has the potential to achieve a more arbitrary selection of chiralities due to the unique band structure of each chirality of nanotubes. Furthermore, sorting SWCNTs directly according to their optoelectronic properties guarantees the optoelectronic properties of the sorted nanotubes and allows only high-quality, defect-free, SWCNTs to be sorted [30].

II. EXPERIMENTAL METHOD

HiPco® SWCNTs (0.01% wt) are suspended in carboxymethyl cellulose solution (1.5% wt). To ensure a large fraction of unbundled nanotubes in the suspension, the suspension is sonicated and centrifuged extensively.

*Present address: School of Physics and Astronomy, University of St. Andrews, St. Andrews, Fife, KY16 9SS Scotland, United Kingdom.
ses12@st-andrews.ac.uk

†Present address: University of Electro-Communication, 1-5-1 Chofugaoka, Chofu, Tokyo 182-8585, Japan.

Initially, the suspension is sonicated, first using a sonic bath for 40 h and then a tip sonicator for 13 h. Overheating of the suspension during tip sonication is prevented by alternating 5-s periods of sonication with 5 s of rest. The carbon nanotube suspension is then centrifuged at 220 000 g for 4 h to remove any bundles of SWCNTs. The upper 50% of the supernatant is removed and subsequently tip sonicated for a further 4 h. The suspension is centrifuged for a second time at 220 000 g for 50 min, and the upper 50% of the supernatant is decanted for use in the experiment.

The SWCNT suspension is confined within a microcapillary chamber. Microcapillaries are fabricated by heating and pulling standard glass capillaries, using a commercially available capillary puller (Narishige, PC-10) to produce long tapers with an inner diameter of approximately 10 μm, an outer diameter of approximately 13 μm, and a length up to 2 cm. The carbon nanotube solution is inserted into the microcapillaries by capillary action. Oil is used to cap the SWCNT suspension at either end of the capillary to create a long, closed, chamber and prevent evaporation.

A continuous-wave Ti:sapphire laser (Spectra Physics, 3900), with the wavelength tunable from 700 to 805 nm and power $P = 100$ mW, is coupled in to one end of the microcapillary by using an $f = 40$ mm lens. The microcapillary acts as a waveguide, guiding the light along the length of the capillary, inside the SWCNT suspension.

Using a typical value for the polarizability of SWCNTs [31], we calculate that resonant nanotubes are pushed by an optical scattering force on the order of 0.1 pN towards the far end of the microcapillary. The experimental setup is shown in Fig. 1.

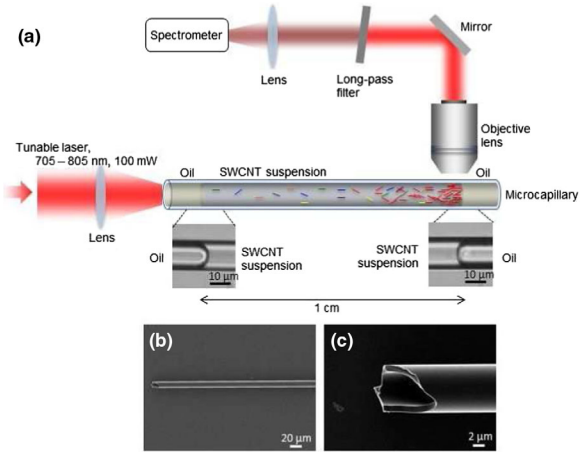

FIG. 1. The experimental setup used. (a) The SWCNT dispersion is confined within a microcapillary chamber. A tunable Ti:sapphire laser (100 mW) is coupled in to one end of the microcapillary. An objective lens collects the Raman scattered light which is analyzed by using a spectrometer. The inset images show optical images of the boundary between the oil and SWCNT suspension at each end of the microcapillary chamber. (b),(c) Scanning-electron-microscope images showing the dimensions of the microcapillary.

Laser light scattered by the SWCNT suspension via resonant Raman scattering is analyzed to provide information on the distribution of nanotube chiralities present in the suspension at the end of the microcapillary. We obtain an accurate measure of the phonon frequencies in the nanotube dispersion, and hence identify the chiralities present, by measuring the intensity of the scattered light as a function of the frequency downshift. We measure the Raman shift caused by the radial breathing mode, the frequency of which is inversely proportional to the tube diameter, thus allowing differentiation of tubes of different diameter and hence chirality [17]. These radial-breathing-mode resonances are radial resonances occurring due to van Hove singularities in the density of states and are not transverse or longitudinal resonances.

The Raman excitation profiles, shown in Figs. 2(a)–2(c), are generated by plotting the amplitude of Lorentzian fits to the Raman spectra versus the excitation wavelength for each Raman frequency shift. By comparing the resonance energy (wavelength for which the Raman peak is maximum) and phonon energy (magnitude of the Raman shift), we assign each peak to specific (n,m) values according to empirical evidence [32,33].

In the experiment wavelength range, we assign peaks to the (8,6), (9,4), (10,2), (12,1), (9,7), and (10,5) chiralities of nanotubes as shown in Fig. 2(d). Figure 2(e) shows the Raman excitation profile of each nanotube chirality that is detected.

After sample characterization, laser light at the pushing wavelength λ_p is coupled in to the capillary and incident on the nanotubes for a period of up to 8 h. To record the time-lapse Raman spectra, the wavelength is temporarily changed to the Raman excitation wavelength λ_{exc} and irradiated on the nanotubes for an integration time of 300 s at intervals of about 1 h. The scattered light is collected by a 20×, NA = 0.6, objective lens and analyzed by using a spectrometer (Princeton Instruments, SpectraPro 300i).

The position and orientation of the nanotubes are governed by Brownian motion and are random. However, during the experiment, the mean force exerted on the carbon nanotubes is in one direction and is strongly dependent on the chirality of the nanotubes. This nonconservative force causes the nanotubes to be pushed in the direction of the laser beam due to the resonant optical force, regardless of the orientation of the nanotube.

We measure the Raman spectra at the far end of the microcapillary and observe a systematic change in the relative amplitudes of the Raman peaks corresponding to different SWCNT chiralities, indicating a local change in the relative densities of different SWCNT chiralities.

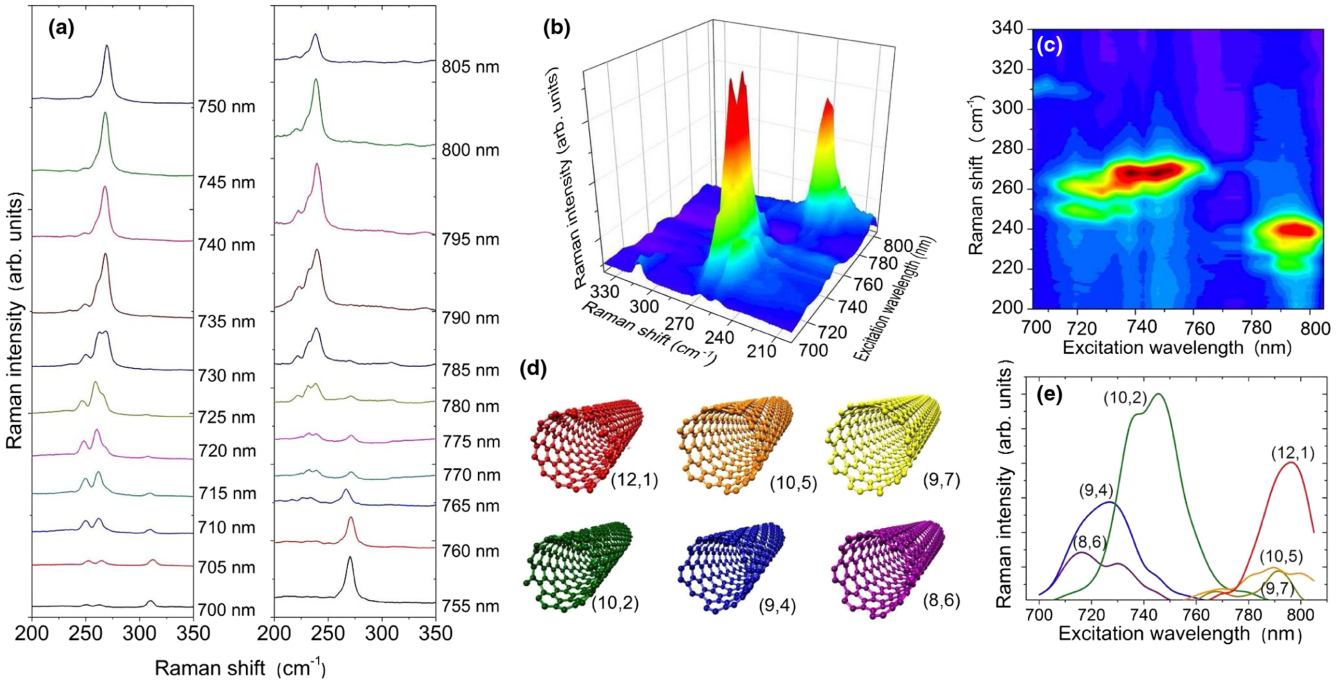

FIG. 2. Experimental spectral characterization of the SWCNT suspension. (a)–(c) Radial-breathing-mode region of the Raman spectrum for an excitation wavelength range 700–805 nm; (d) the SWCNT chiralities detected in our experiment: (12,1), (10,5), (9,7), (10,2), (9,4), and (8,6); (e) measured Raman excitation profiles for the same SWCNT chiralities.

III. RESULTS AND DISCUSSION

Figures 3(a)–3(e) show time-lapse Raman spectra measured at the end of the capillary by using a Raman excitation wavelength of $\lambda_{\mathrm{exc}} = 775$ nm and an optical pushing wavelength of $\lambda_p = 795$ nm. The Raman peak assigned to the (10,2) chirality increases over a period of 8 h of laser irradiation. Figure 3(f) shows the ratios of the height of each peak (chirality) versus the cumulative pushing time. The peak corresponding to (10,2) SWCNTs increases linearly, compared to the other peaks, corresponding to (9,7), (10,5), and (12,1) nanotubes, for which the gradients of the fitted lines are zero within the error bars.

By changing the pushing wavelength to $\lambda_p = 805$ nm and using the same Raman excitation wavelength of $\lambda_{\mathrm{exc}} = 775$ nm, a different chirality of nanotube is pushed by the laser beam. At this wavelength, the peak corresponding to the (12,1) chirality increases, while the relative heights of the other peaks remain constant, as shown in Fig. 4.

Using a wavelength of $\lambda_p = 740$ nm results in optical pushing of both the (8,6) and (9,4) nanotubes, as shown in Fig. 5. To obtain Raman spectra of these tubes, a Raman excitation wavelength of $\lambda_{\mathrm{exc}} = 730$ nm is used. From the gradients of the time-dependent peak ratio graphs in Figs. 5(e) and 5(f), it is evident that both peaks increase at the same rate.

For all three optical pushing wavelengths shown above, the resonant optical scattering force wavelengths are redshifted from the peak in the Raman excitation profile for each SWCNT chirality [Fig. 2(e)]. For example, the wavelength used to successfully push (10,2) SWCNTs is $\lambda_p = 795$ nm, while the Raman excitation peak is centered around 740 nm. For (12,1) nanotubes, the pushing wavelength is $\lambda_p = 805$ nm, while the Raman peak is centered around 798 nm. Chiralities (8,6) and (9,4), which both have Raman peaks centered around 725 nm, are pushed with a wavelength of $\lambda_p = 740$ nm.

A qualitative understanding of the reasons for this redshift can be gained by considering the mechanisms behind the Raman scattering process and the optical scattering force on nanotubes and the relationship between these processes and the polarizability of the nanotubes. An intuitive understanding of the relationship between the optical scattering force and the polarizability can be gained by considering the optical forces in the dipole approximation [34], where the time-averaged force acting on a SWCNT can be expressed as [35]

$$\langle F \rangle = \frac{1}{2}\mathrm{Re}\left(\sum_{j=x,y,z} \alpha(\lambda) E_j \nabla E_j^* \right), \tag{1}$$

where $\alpha(\lambda)$ is the wavelength-dependent polarizability and E_j are the electric field components. By rearranging, neglecting the terms relating to the gradient and spin-curl forces due to the low numerical aperture of the microcapillary, and substituting for the extinction cross section [21], the wavelength dependence of the scattering force varies as

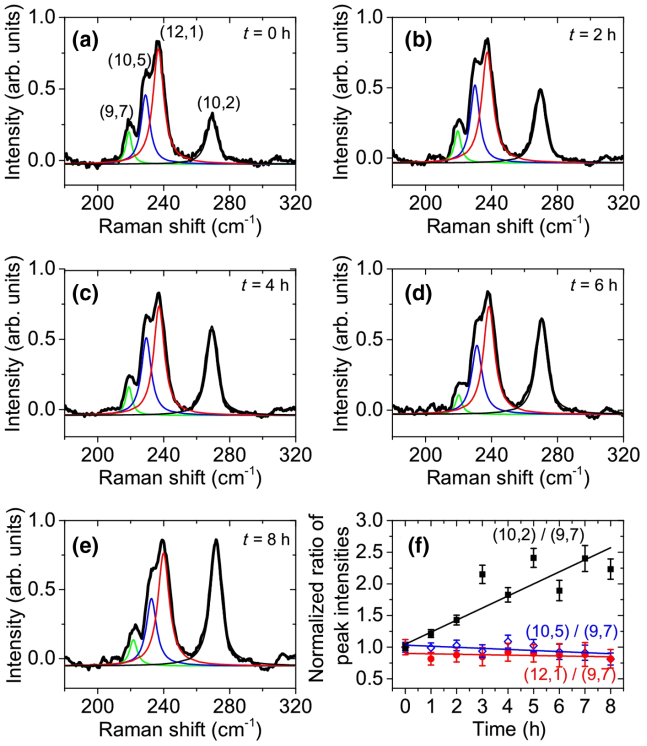

FIG. 3. Raman data obtained by using a Raman excitation wavelength $\lambda_{\mathrm{exc}} = 775$ nm and an optical pushing wavelength $\lambda_p = 795$ nm. (a)–(e) Time-lapse Raman spectra obtained at the far end of the microcapillary. The thick black line shows the raw Raman spectra; the thinner colored curves show Lorentzian fits to the Raman peaks. (f) Ratios of the height of the Lorentzian fits of the (10,2) (black), (10,5) (blue), and (12,1) (red) nanotubes, normalized by the height of the (9,7) chirality peak, versus the pushing time. The ratios are normalized to the initial ratio at $t = 0$ h. The error bars are derived from the errors in the fits.

$$\langle F_{\mathrm{scat}}(\lambda)\rangle = \left(\frac{A}{\lambda}\mathrm{Im}[\alpha(\lambda)] + \frac{B}{\lambda^4}|\alpha(\lambda)|^2\right)\mathrm{Re}(\mathbf{E}\times\mathbf{H}^*), \quad (2)$$

where $\mathbf{E}$ is the electric field, $\mathbf{H}$ is the magnetic field, and A and B are constants. Equation (2) shows that the optical scattering force on the nanotubes depends on both the real and imaginary parts of the polarizability. In contrast, the excitation wavelength which results in maximum Raman scattering is proportional only to the imaginary component of the polarizability [17]. The peak of the real component of the polarizability is redshifted with respect to the peak of the imaginary component, as defined by the Kramers-Krönig relation [36]; hence, the wavelength for the resonant optical scattering force is redshifted with respect to the Raman excitation wavelength.

Although our method provides significant chirality enrichment, it will not give 100% chiral purity. Figures 3–5 show a linear dependence of the normalized ratio of peak intensities on time. However, we expect there to be a saturating limit determined by parameters including the temperature of the suspension, the optical intensity, the

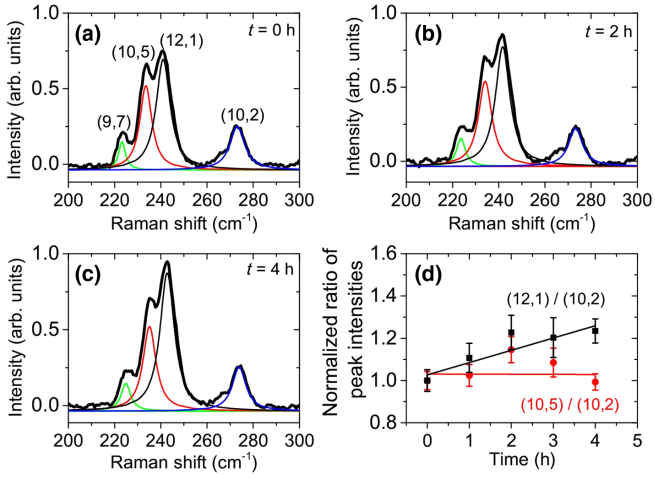

FIG. 4. Raman data obtained by using a Raman excitation wavelength $\lambda_{\mathrm{exc}} = 775$ nm and an optical pushing wavelength $\lambda_p = 805$ nm. (a)–(c) Time-lapse Raman spectra obtained at the far end of the microcapillary. (d) Ratios of the height of the Lorentzian fits of the (12,1) (black) and (10,5) (red) nanotubes, normalized by the height of the (10,2) chirality peak, versus the pushing time. The ratios are normalized to the initial ratio at $t = 0$ h. The error bars are derived from the errors in the fits.

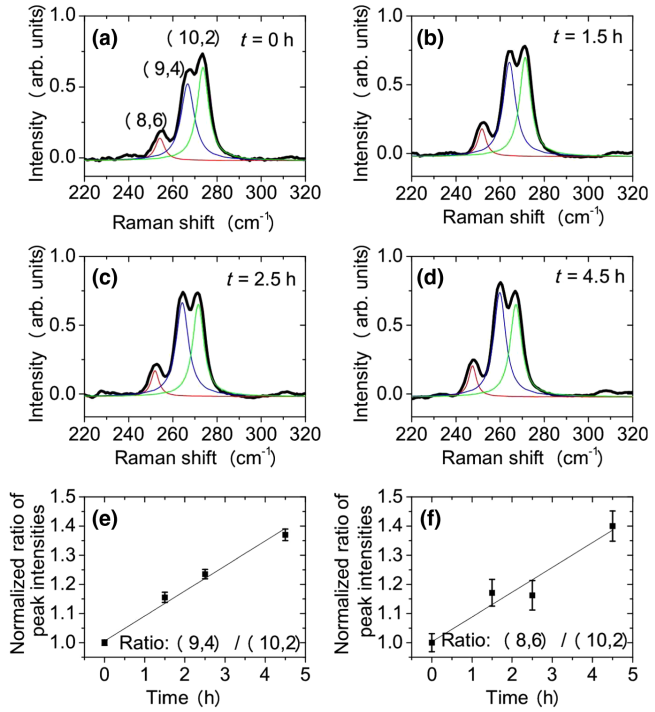

FIG. 5. Raman data obtained by using a Raman excitation wavelength $\lambda_{\mathrm{exc}} = 730$ nm and an optical pushing wavelength $\lambda_p = 740$ nm. (a)–(d) Time-lapse Raman spectra obtained at the far end of the microcapillary. (e) Ratios of the height of the Lorentzian fits of the (9,4) to the (10,2) chirality peak versus the pushing time. (f) Ratios of the height of the Lorentzian fits of the (8,6) to the (10,2) chirality peak versus the pushing time. The ratios are normalized to the initial ratio at $t = 0$ h. The error bars are derived from the errors in the fits.

overlap in resonances, the dimensions of the capillary, and the initial relative concentrations of nanotubes with different chiral vectors. Increased chiral purity could be achieved by extending the method to include counterpropagating laser beams with different wavelengths to push nanotubes with one chiral vector in the opposite direction to nanotubes with all other chiral vectors.

We note that the resonance wavelength of the nanotubes depends solely on the diameter of the nanotubes and that differing lengths would not lead to broadening of the resonances. However, in the limit where nanotubes become so short that they cannot sustain a rigid identical chirality in the molecular structure, then they will not be sorted. Indeed, this is one of the strengths of our method, as the sorting mechanism depends directly on the optoelectronic properties, so only complete and nondamaged tubes will be sorted from the population. However, shorter nanotubes are likely to experience a lower frictional drag force, and therefore we expect resonant nanotubes to also be separated based on length.

IV. CONCLUSION

In conclusion, we experimentally demonstrate a wavelength-dependent, chirality-selective, optical scattering force on SWCNTs. By tuning the wavelength of the laser beam to match the resonant conditions of each chirality of nanotube, we achieve selective enrichment of four chiralities of SWCNTs. We predict that this result will lead to the implementation of optical techniques for the chirality-based optical sorting and manipulation of carbon nanotubes, allowing homogeneous dispersions of nanotubes with well-defined optoelectronic properties to be directly sorted from a polydisperse population.

Although separation took several hours in our experiment, faster separation rates may be achieved by increasing the optical power, which was only limited here due to boiling of the oil used to cap each end of the microcapillary. Moreover, further characterization of the optical scattering force on nanotubes and optimization of the choice of wavelength to achieve maximum force on each chirality of nanotubes is expected to increase the efficiency and rate of chirality separation.

Further optimization of the geometry of the chamber, for example, by using an appropriately designed microfluidic chip, is expected to facilitate the sorting of much larger volumes of nanotube suspension. It may also allow a population to be separated into multiple pure samples containing nanotubes of differing chiralities. Furthermore, in addition to sorting nanotubes based solely on their chiral vector, the implementation of circular polarization could be used to differentiate between nanotubes with the same chiral vector but opposite handedness.

ACKNOWLEDGMENTS

This research is supported by The Canon Foundation and KAKENHI Grant-in-Aid for Young Scientists, MEXT, Japan. The authors thank Osaka University Photonics Center for financial support and the loan of equipment and Kenji Asaba and Ikki Kousaka for their assistance with early aspects of the project.

[1] T. Ueda, M. M. H. Bhuiyan, H. Norimatsu, S. Katsuki, T. Ikegami, and F. Mitsugi, Development of carbon nanotube-based gas sensors for NOx gas detection working at low temperature, Physica (Amsterdam) E **40**, 2272 (2008).

[2] Z. Zanolli, R. Leghrib, A. Felten, J.-J. Pireaux, E. Llobet, and J.-C. Charlier, Gas sensing with Au-decorated carbon nanotubes, ACS Nano **5**, 4592 (2011).

[3] E. Poirier, R. Chahine, P. Bénard, D. Cossement, L. Lafi, E. Mélançon, T. K. Bose, and S. Désilets, Storage of hydrogen on single-walled carbon nanotubes and other carbon structures, Appl. Phys. A **78**, 961 (2004).

[4] B. Panella, M. Hirscher, and S. Roth, Hydrogen adsorption in different carbon nanostructures, Carbon **43**, 2209 (2005).

[5] P.-J. Tsai, C.-H. Yang, W.-C. Hsu, W.-T. Tsai, and J.-K. Chang, Enhancing hydrogen storage on carbon nanotubes via hybrid chemical etching and pt decoration employing supercritical carbon dioxide fluid, Int. J. Hydrogen Energy **37**, 6714 (2012).

[6] Y. Jia, A. Cao, X. Bai, Z. Li, L. Zhang, N. Guo, J. Wei, K. Wang, H. Zhu, D. Wu, and P. M. Ajayan, Achieving high efficiency silicon-carbon nanotube heterojunction solar cells by acid doping, Nano Lett. **11**, 1901 (2011).

[7] D. D. Tune, B. S. Flavel, R. Krupke, and J. G. Shapter, Carbon nanotube-silicon solar cells, Adv. Energy Mater. **2**, 1043 (2012).

[8] P. Avouris, Z. Chen, and V. Perebeinos, Carbon-based electronics, Nat. Nanotechnol. **2**, 605 (2007).

[9] M. L. Geier, P. L. Prabhumirashi, J. J. McMorrow, W. Xu, J.-W. T. Seo, K. Everaerts, C. H. Kim, T. J. Marks, and M. C. Hersam, Subnanowatt carbon nanotube complementary logic enabled by threshold voltage control, Nano Lett. **13**, 4810 (2013).

[10] D.-M. Sun, C. Liu, W.-C. Ren, and H.-M. Cheng, A review of carbon nanotube- and graphene-based flexible thin-film transistors, Small **9**, 1188 (2013).

[11] C. Wang, K. Takei, T. Takahashi, and A. Javey, Carbon nanotube electronics—Moving forward, Chem. Soc. Rev. **42**, 2592 (2013).

[12] M. M. Shulaker, G. Hills, N. Patil, H. Wei, H.-Y. Chen, H.-S. P. Wong, and S. Mitra, Carbon nanotube computer, Nature (London) **501**, 526 (2013).

[13] A. Vijayaraghavan, Applications of chirality-sorted individual single-wall carbon nanotube devices, J. Mater. Chem. **22**, 7083 (2012).

[14] J.-C. Charlier, X. Blase, and S. Roche, Electronic and transport properties of nanotubes, Rev. Mod. Phys. **79**, 677 (2007).

[15] T. Ando, Theory of electronic states and transport in carbon nanotubes, J. Phys. Soc. Jpn. **74**, 777 (2005).

[16] A. Jorio, A. G. Souza Filho, G. Dresselhaus, M. S. Dresselhaus, R. Saito, J. H. Hafner, C. M. Lieber, F. M. Matinaga, M. S. S. Dantas, and M. A. Pimenta, Joint density of electronic states for one isolated single-wall carbon nanotube studied by resonant Raman scattering, Phys. Rev. B **63**, 245416 (2001).

[17] M. S. Dresselhaus, G. Dresselhaus, R. Saito, and A. Jorio, Raman spectroscopy of carbon nanotubes, Phys. Rep. **409**, 47 (2005).

[18] T. Imasaka, Y. Kawabata, T. Kaneta, and Y. Ishidzu, Optical chromatography, Anal. Chem. **67**, 1763 (1995).

[19] M. P. MacDonald, G. C. Spalding, and K. Dholakia, Microfluidic sorting in an optical lattice, Nature (London) **426**, 421 (2003).

[20] M. Ploschner, T. Cizmar, M. Mazilu, A. Di Falco, and K. Dholakia, Bidirectional optical sorting of gold nanoparticles, Nano Lett. **12**, 1923 (2012).

[21] S. E. Skelton, M. Sergides, R. Patel, E. Karczewska, O. M. Maragó, and P. H. Jones, Evanescent wave optical trapping and transport of micro-and nanoparticles on tapered optical fibers, J. Quant. Spectrosc. Radiat. Transfer **113**, 2512 (2012).

[22] T. Rodgers, S. Shoji, Z. Sekkat, and S. Kawata, Selective Aggregation of Single-Walled Carbon Nanotubes Using the Large Optical Field Gradient of a Focused Laser Beam, Phys. Rev. Lett. **101**, 127402 (2008).

[23] M. S. Arnold, A. A. Green, J. F. Hulvat, S. I. Stupp, and M. C. Hersam, Sorting carbon nanotubes by electronic structure using density differentiation, Nat. Nanotechnol. **1**, 60 (2006).

[24] M. S. Arnold, S. I. Stupp, and M. C. Hersam, Enrichment of single-walled carbon nanotubes by diameter in density gradients, Nano Lett. **5**, 713 (2005).

[25] S. Ghosh, S. M. Bachilo, and R. B. Weisman, Advanced sorting of single-walled carbon nanotubes by nonlinear density-gradient ultracentrifugation, Nat. Nanotechnol. **5**, 443 (2010).

[26] X. Tu, S. Manohar, A. Jagota, and M. Zheng, DNA sequence motifs for structure-specific recognition and separation of carbon nanotubes, Nature (London) **460**, 250 (2009).

[27] H. Liu, D. Nishide, T. Tanaka, and H. Kataura, Large-scale single-chirality separation of single-wall carbon nanotubes by simple gel chromatography, Nat. Commun. **2**, 309 (2011).

[28] M. Zheng, A. Jagota, M. S. Strano, A. P. Santos, P. Barone, S. G. Chou, B. A. Diner, M. S. Dresselhaus, R. S. Mclean, G. B. Onoa, G. G. Samsonidze, E. D. Semke, M. Usrey, and D. J. Walls, Structure-based carbon nanotube sorting by sequence-dependent dna assembly, Science **302**, 1545 (2003).

[29] A. Nish, J.-Y. Hwang, J. Doig, and R. J. Nicholas, Highly selective dispersion of single-walled carbon nanotubes using aromatic polymers, Nat. Nanotechnol. **2**, 640 (2007).

[30] D. Smith, C. Woods, A. Seddon, and H. Hoerber, Photophoretic separation of single-walled carbon nanotubes: A novel approach to selective chiral sorting, Phys. Chem. Chem. Phys. **16**, 5221 (2014).

[31] G. Y. Slepyan, M. V. Shuba, S. A. Maksimenko, and A. Lakhtakia, Theory of optical scattering by achiral carbon nanotubes and their potential as optical nano antennas, Phys. Rev. B **73**, 195416 (2006).

[32] S. K. Doorn, D. A. Heller, P. W. Barone, M. L. Usrey, and M. S. Strano, Resonant Raman excitation profiles of individually dispersed single walled carbon nanotubes in solution, Appl. Phys. A **78**, 1147 (2004).

[33] R. B. Weisman and S. M. Bachilo, Dependence of optical transition energies on structure for single-walled carbon nanotubes in aqueous suspension: An empirical Kataura plot, Nano Lett. **3**, 1235 (2003).

[34] O. M. Maragó, P. H. Jones, P. G. Gucciardi, G. Volpe, and A. C. Ferrari, Optical trapping and manipulation of nano structures, Nat. Nanotechnol. **8**, 807 (2013).

[35] P. C. Chaumet and M. Nieto-Vesperinas, Time-averaged total force on a dipolar sphere in an electromagnetic field, Opt. Lett. **25**, 1065 (2000).

[36] J. S. Toll, Causality and the dispersion relation: Logical foundations, Phys. Rev. **104**, 1760 (1956).